Applied Surface Science 574 (2022) 151633

Contents lists available at ScienceDirect

Applied Surface Science

journal homepage: www.elsevier.com/locate/apsusc

Full Length Article

Palladium-graphene hybrid as an electrocatalyst for hydrogen peroxide reduction

Jelena Čović [a,*], Valentin Mirceski [b,c], Aleksandra Zarubica [a], Dirk Enke [d], Simon Carstens [d], Aleksandar Bojić [a], Marjan Ranđelović [a]

[a] University of Niš, Faculty of Sciences and Mathematics, Department of Chemistry, 33 Višegradska St., 18000 Niš, Serbia
[b] Faculty of Chemistry, Department of Inorganic and Analytical Chemistry, University of Lodz, Tamka 12, 91–403 Lodz, Poland
[c] Institute of Chemistry, Faculty of Natural Sciences and Mathematics, Ss. Cyril and Methodius University, Arhimedova 5, 1000 Skopje, Macedonia
[d] Institut für Technische Chemie, Universität Leipzig, Raum 515a, Linnéstr. 3, D-04103 Leipzig, Germany

ARTICLE INFO

Keywords:
Hydrogen peroxide reduction reaction
Electrocatalysis
Hybrid material
Palladium
Graphene

ABSTRACT

The electrocatalytic reduction of hydrogen peroxide in an alkaline solution has been studied on a hybrid material based on hydrothermally obtained palladium particles supported on graphene (Pd@G). The morphology, structure, and chemical composition of the prepared hybrid material, including spatial distribution of palladium nanoparticles, were examined by SEM, XRD, EDX, elemental mapping, XPS, FTIR, and BET. The hydrogen peroxide reduction reaction (HPRR) was studied by cyclic and square wave voltammetry in an oxygen-free and air-saturated alkaline medium. The Pd@G exhibited pronounced electrocatalytic activity for HPRR, which proceeds via complex electrode mechanisms coupled with adsorption phenomena and hydrogen peroxide disproportionation reaction as a heterogeneous chemical process on the surface of palladium nanoparticles.

1. Introduction

Hydrogen peroxide (H_2O_2) is a simple molecule known for its oxidizing and reducing properties. It is being widely used in various industrial fields related to the environment, pharmacy, textile, paper, fuel cells, and food [1]. Due to its high importance, the hydrogen peroxide reduction reaction (HPRR) is extensively studied, particularly focusing on analytical and other applications. Hydrogen peroxide is a weak acid (pK_a 11.7) that dissociates in alkaline media generating a perhydroxyl anion, which dominates as the most stable form [2–4].

$$H_2O_2 + OH^- \leftrightarrows HO_2^- + H_2O$$

Some earlier studies suggest that H_2O_2 undergoes catalytic decomposition on noble metals forming oxygen, which can be reduced back to hydrogen peroxide [4–5]. Hence, revealing the mechanism of the HPRR process in alkaline solutions is rather challenging, as it may occur through one of the following three pathways [6].

(1) Electrochemical reaction mechanism through direct reduction of H_2O_2 to hydroxyl ion:
$HO_2^- + H_2O + 2e^- \leftrightarrows 3OH^-$ $\quad E^0 = 0.878$ V vs. SHE

(2) Chemical-electrochemical reaction mechanism (CE) by the decomposition of H_2O_2 to O_2, which reduces back to peroxide:
$2HO_2^- \rightarrow O_2 + 2OH^-$
$O_2 + H_2O + 2e^- \leftrightarrows HO_2^- + OH^-$ $\quad E^0 = -0.076$ V vs. SHE (alkaline media)

(3) A combination of paths 1 and 2 [7].

Nanostructures based on metal and carbon NPs, conventionally called “hybrids”, have attracted significant attention among different electrode materials for HPRR. The International Union of Pure and Applied Chemistry (IUPAC) defines them as “multicomponent materials comprising multiple, different (non-gaseous) phase domains in which at least one type of phase domain is a continuous phase” [8]. Up to date, many hybrid materials have been synthesized considering their favourable characteristics associated with a nano-size effect and their specific heterogeneous structure with intimate contact between chemically and physically very different constituents. These materials have been increasingly employed in electrocatalysis and electroanalysis due to their pronounced electrocatalytic effects [9–15]. In the light of electrochemistry, the proximity of different atoms may induce interesting co-catalytic effects of hybrids and promote charge transfer through more

* Corresponding author.
E-mail address: covic.jelena91@gmail.com (J. Čović).

https://doi.org/10.1016/j.apsusc.2021.151633
Received 21 June 2021; Received in revised form 13 October 2021; Accepted 14 October 2021
Available online 20 October 2021

favourable pathways. Recently, an increasing number of research and review papers covering graphene-based hybrids have been reported [16–19]. Noble metal nanoparticles such as Pt, Pd, Cu, Ag, and Au have been frequently used for modification of the working electrode surface, due to their large surface area, long-term stability, and high conductivity [20–22].

Several studies examine hybrid materials composed of graphene oxide and Pd or Pd-based alloys for hydrogen peroxide reduction in phosphate buffer (pH ≈ 7) as supporting electrolytes [23–26]. However, a study that involves the large-scale preparation of graphene subsequently modified with palladium nanoparticles by a hydrothermal method has not been reported so far. Therefore, we report herein the synthesis of graphene (G) which is decorated with palladium (Pd) nanoparticles (Pd@G) as an efficient hybrid electrocatalyst for electrochemical reduction of hydrogen peroxide (H_2O_2) in an alkaline medium. Palladium particles were partially segregated on the surface of graphene, achieving their favourable distribution for efficient electrocatalysis. The resulting Pd@G hybrid material was characterized by SEM, EDX, XRD, XPS, FTIR, and BET. The electroreduction reaction of H_2O_2 on Pd@G was studied by cyclic voltammetry (CV) and square wave voltammetry (SWV) in both the presence and absence of oxygen, aiming to unveil the main aspects of the electrocatalytic mechanism.

2. Experimental

2.1. Synthesis of graphene (G)

The preparation procedure of graphene was adapted from the previously reported method by Zhang et al. [27]. 6.00 g of glucose and 6.00 g of $FeCl_3{\cdot}6H_2O$ were dissolved in 10 mL of deionized water. Water evaporation was carried out by heating at 80 °C for 24 h. Carbonization of the obtained product was performed at 700 °C for 3 h under an inert atmosphere of nitrogen. Subsequently, the material was ground, transferred into 100 mL of conc. HCl (36%) and stirred for 6 h. Afterward, the suspension was filtered and washed with 300 mL deionized water and 80 mL acetone. The obtained material was dried at 70 °C for 1 h.

2.2. Synthesis of palladium-graphene hybrid (Pd@G)

100 mg of graphene were dispersed in 20 mL of an ethanol/water mixture (50%, *v/v*) and sonicated for 5 min. Then 25 mg of cetyltrimethylammonium bromide (CTAB) were added and the sonication was continued for another 5 min. 50 mg of $PdCl_2$ and 0.05 mL conc. HCl were placed in a test tube and heated at 60 °C for 30 min. After cooling the solution was diluted with H_2O to 2 mL and added to the graphene suspension. It was left at room temperature for 1 h before 1 mL of $NaBH_4$ was added. The obtained suspension was then transferred into a stainless steel autoclave and heated at 160 °C for 90 min. After hydrothermal treatment, the obtained suspension was centrifuged, and the liquid phase was decanted. The residue was washed several times with deionized water. Finally, the obtained material was dried at 60 °C and denoted as Pd@G. For comparison, corresponding palladium deposition was carried out onto commercial graphene (Acros Organics) following the same procedure as described above, and the obtained hybrid material is denoted as Pd-commercial G.

2.3. Electrode preparation

Firstly, a glassy carbon electrode (GCE) (with a geometrical area of 0.0706 cm^2) was polished on a polishing cloth with 0.05 μm Al_2O_3 powder slurry, rinsed with deionized water, and flushed with ethanol in an ultrasonic bath. Following the cleaning procedure, 5 mg of G or Pd@G were dispersed in 1 mL of an ethanol/water mixture (40%, *v/v*), and the obtained suspension was homogenized in an ultrasonic bath for 30 min. 5 μL of the suspension (corresponding to 0.025 mg of the material) were transferred onto the surface of the GCE and dried under N_2 stream. After the thin layer of electrocatalyst was formed, it was covered with 5 μL of 0.05 wt% Nafion solution in ethanol and dried again under N_2 stream. The modified GCE was used for studying the electroreduction of H_2O_2. The nominal metal loading for Pd-based electrocatalysts was calculated to be 82 μg cm^{-2}. The Nafion thickness was estimated to be approximately 0.2 μm, according to the following Eq. (1).

$$t = m/(A\rho) \quad (1)$$

where m is the mass of drop cast Nafion ($2.500{\cdot}10^{-6}$ g), A is the area of the film, and ρ is the approximate density of the film (1.980 g cm^{-3}).

Worth noting is that oxygen and hydrogen peroxide are capable to permeate Nafion membranes of a few microns and thus can be reduced at the electrode surface [28]. The electroreduction of H_2O_2 was studied by CV and SWV within the potential range from +0.200 to −0.600 V.

A three-electrode system consisted of Pd@G modified GCE as a working electrode, a saturated calomel electrode (SCE) as a reference, and a graphite bar or platinum coil was used as an auxiliary electrode. Typically, the solution of 5 mM H_2O_2 in 0.1 M KOH was used to examine the electrocatalytic behaviour of Pd@G. Purified nitrogen was bubbled through the supporting electrolyte for thirty minutes. Then the proper quantity of hydrogen peroxide was added. The electrolytic cell was protected from light by Al-foil. Before electrochemical measurements, activation of each electrocatalytic film was performed by continuously cycling the potential (10 cycles) from −0.600 V to +0.200 V vs. SCE in an N_2-saturated 0.1 M KOH solution until a stable reproducible cyclic voltammogram was recorded. Some measurements were carried out in air-saturated electrolytes, as specified in the following sections.

2.4. Characterization

Nanohybrid Pd@G material was characterized by scanning electron microscopy (SEM), and X-ray powder diffraction (XRD), X-ray photoelectron spectroscopy (XPS), Fourier Transform Infrared Spectroscopy (FTIR), and BET nitrogen adsorption and desorption analysis. SEM images were obtained using a Leo Gemini 1530 device by Zeiss with an Everhart-Thornley detector for collecting secondary electrons. The accelerating voltage was 10 kV. Powder XRD of the finely ground samples was measured on a STADI P instrument from STOE & Cie GmbH with a Mythen1K detector. Cu-Kα-radiation was used at 40 kV and 40 mA. XPS was performed using SPECS Systems with XP50M X-ray source for Focus 500 and PHOIBOS 100/150 analyzer. AlKα source (1486.74 eV) at a 12.5 kV and 32 mA was used. FTIR spectroscopy was carried out by using an FTIR spectrometer (Bomem MB-100, Hartmann & Braun, Canada). Brunauer-Emmett-Teller (BET) specific surface area analysis was carried out on an Autosorb iQ by 3P instruments. The sample was analyzed under a nitrogen atmosphere.

3. Results

3.1. XRD

The crystalline structure and average crystallite size of graphene (G) and Pd@G nanocomposite were defined using XRD (Fig. 1).

3.2. Morphological characterization and EDX

The morphology of G and Pd@G nanocomposite were analyzed using SEM and the corresponding microphotographs are given in Fig. 2a and b, respectively. The chemical composition, concentration, and distribution of elements for G and Pd@G were determined using energy-dispersive X-ray spectroscopy (EDX). EDX spectra of G and Pd@G with corresponding peaks are presented in Fig. 2c and d, respectively. The distribution of some elements in the samples of G and Pd@G are given in Fig. 2e–g. The distribution of Fe in G and Pd@G samples are presented in Fig. 2e–g, respectively, and the distribution of Pd in the Pd@G sample is given in

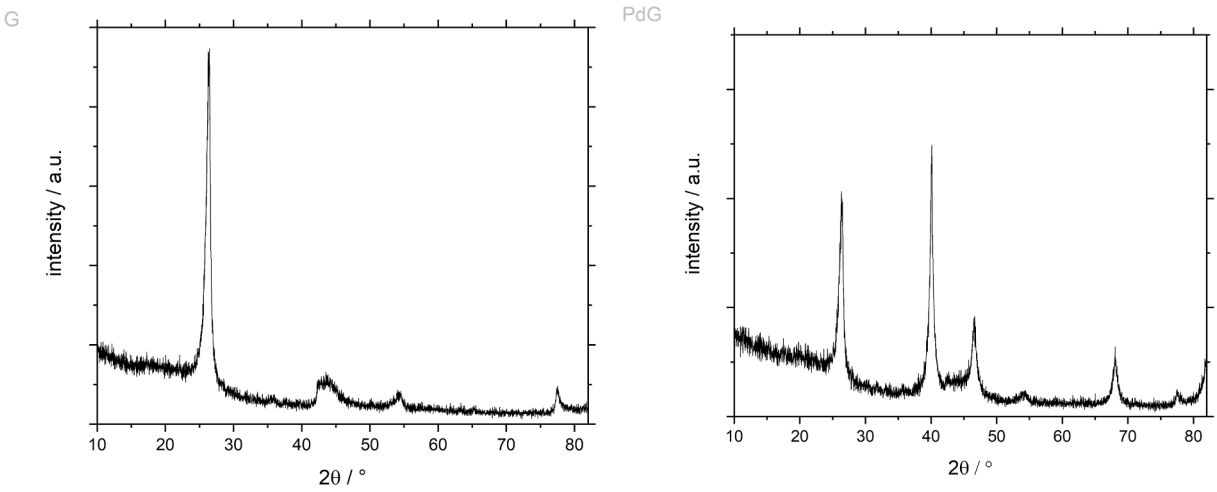

Fig. 1. XRD pattern of graphene (G) (left) and Pd@G hybrid (right).

Fig. 2f.

3.3. XPS

X-ray photoelectron spectroscopy (XPS) was used to determine the surface elemental compositions and chemical oxidation states of Pd in the Pd@G sample. XPS spectra (0–1000 eV binding energy) were recorded with a constant pass energy of 40 eV, step size of 0.5 eV, and dwell time of 0.2 s in the FAT mode, while detailed spectra were recorded with the following values of parameters: constant pass energy of 20 eV, step size of 0.1 eV and dwell time of 0.2 s in FAT mode, at a pressure of 9×10^{-9} mbar.

The obtained spectra are given in Fig. 3.

3.4. FTIR spectroscopy

The infrared spectra of G and Pd@G nanocomposite in the 400–4000 cm^{-1} range are displayed in Fig. 4a and b, respectively.

3.5. BET analysis

Prior to the examination, the samples were dried, outgassed, and activated at 300 °C under vacuum. Determination of the specific surface area (ABET) was conducted using the linearized form of the BET equation in the range of $0.05 \leq p/p0 \leq 0.30$.

3.6. HPRR (hydrogen peroxide reduction reaction)

The HPRR mechanism was studied by applying cyclic voltammetry and square voltammetry in an alkaline medium. Initially, cyclic voltammograms of 5 mM H_2O_2 were recorded in a degassed 0.1 M KOH solution within the potential interval from +0.200 V to −0.600 V (vs. SCE) to examine preliminary reaction kinetics at GC, G, Pd@G, and Pd-commercial G electrodes. Fig. 5a and b depict cyclic voltammograms at a scan rate of 10 mV s^{-1} both in the absence and the presence of 5 mM H_2O_2, respectively. The initial study of the Pd-commercial G electrode revealed a rather poor electrocatalytic activity; thus, this material was excluded from further examination.

The voltammetric data in Fig. 5 reveal a superior electrocatalytic activity of the Pd@G electrode [29]. The shape of the cyclic voltammogram of the Pd@G electrode in a blank 0.1 M KOH solution (i.e., containing neither dissolved oxygen nor added H_2O_2) (Fig. 5a) features a well-developed cathodic voltammetric peak, which is ascribed to the reduction of oxygen traces adsorbed on the Pd-particles. In-depth inspection of the peak morphology reveals that it is composed of two overlapping peaks positioned at about −0.200 V and −0.270 V. Thus, the reduction of oxygen at the Pd@G electrode can be assumed to proceed as a two-step process of adsorbed species, giving rise to the voltammetric peaks at about −0.200 V and −0.270 V. The process commences with adsorbed oxygen (O_2(ads)), proceeding via electrochemical formation of adsorbed hydrogen peroxide, followed by further reduction of H_2O_2(ads) to, most probably, adsorbed hydroxide ions [6–7]. Integrating the overall cathodic peak of the cyclic voltammogram at Pd@G electrode (Fig. 5a) yields the charge value of $Q = 2.77 \cdot 10^{-2}$ C. Thus, in a first approximation, the surface concentration of the oxygen adsorbed on Pd particles can be calculated as:

$$\Gamma = Q/(nFA) \tag{2}$$

where $n = 4$ is the stoichiometric number of electrons, F is the Faraday constant, and $A = 0.071$ cm^2 is the geometric surface area of the working electrode. The apparent surface coverage of the Pd@G electrode with adsorbed oxygen was calculated to be 1.020 μmol cm^{-2}, indicating a large active surface area of Pd electrocatalytic nanoparticles and a strong adsorption affinity of oxygen [7,14]. It is worth mentioning that in the anodic part of the same voltammogram (Fig. 5a, Pd@G electrode), an oxidation process takes place at about 0.100 V, which can be ascribed to OH^-(ads) catalytic oxidation or Pd oxide formation [7,30]. The oxidation products of the latter anodic process cause a slight bulge in the cathodic region of cyclic voltammograms upon repetitive cycling of the potential (data not shown).

The Pd@G electrode exhibits a strong reductive peak in the presence of 5 mM H_2O_2 in a degassed solution at the scan rate of $v = 10$ mV s^{-1} (Fig. 5b), being significantly higher compared to all other studied electrodes. The cathodic peak is associated with the peak current of $I_p = -1075$ μA, while the peak potential ($E_p = -0.270$ V) corresponds to the position of the main reduction peak in Fig. 5a. The corresponding cathodic peaks at graphene-modified and bare glassy carbon electrodes are strongly diminished compared to the Pg@G electrode, being significantly shifted in the cathodic direction with corresponding peak potentials of −0.400 V and −0.480 V, respectively (Table 1).

Further assessment of the electrode kinetics has been conducted by Tafel analysis, by processing the initial raising part of cyclic voltammograms recorded at $v = 10$ mV s^{-1}, and corresponding data are summarized in Table 1 and Fig. S1. The reaction kinetics was evaluated applying the derived Tafel equations as follows [31–32]:

$$\eta = a + b\log(i) \tag{3}$$

$$b = -2.3RT/(\alpha nF) \tag{4}$$

where η is the overpotential, which presents the difference between the

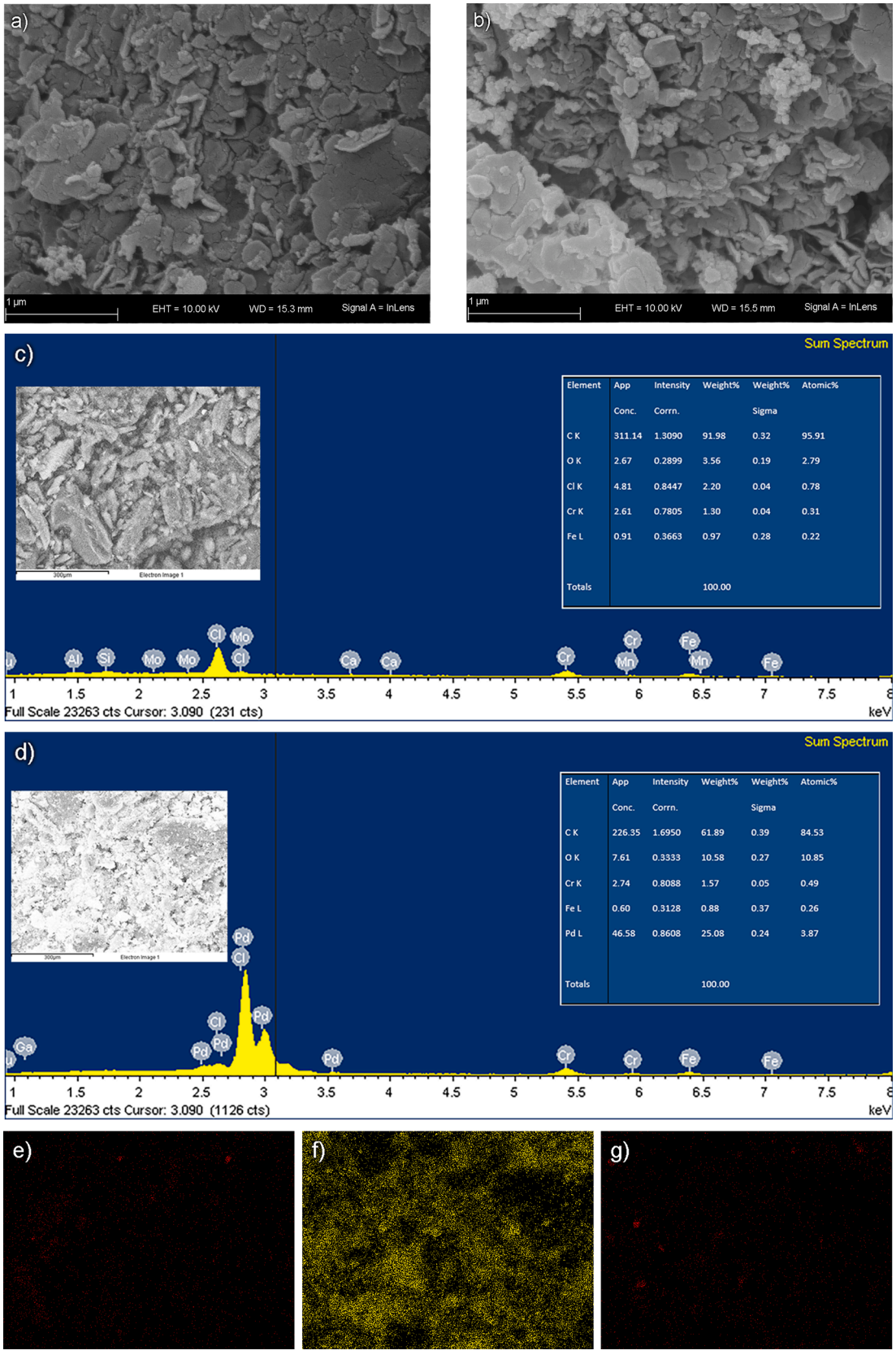

Fig. 2. SEM microphotographs of (***a***) G and (***b***) Pd@G; EDX spectra of (***c***) G and (***d***) Pd@G; the insets in (***c***) and (***d***) show the elemental composition of G and Pd@G, respectively; EDX elemental maps of (***e***) Fe in G sample, (***f***) Pd in Pd@G sample and (***g***) Fe in Pd@G sample.

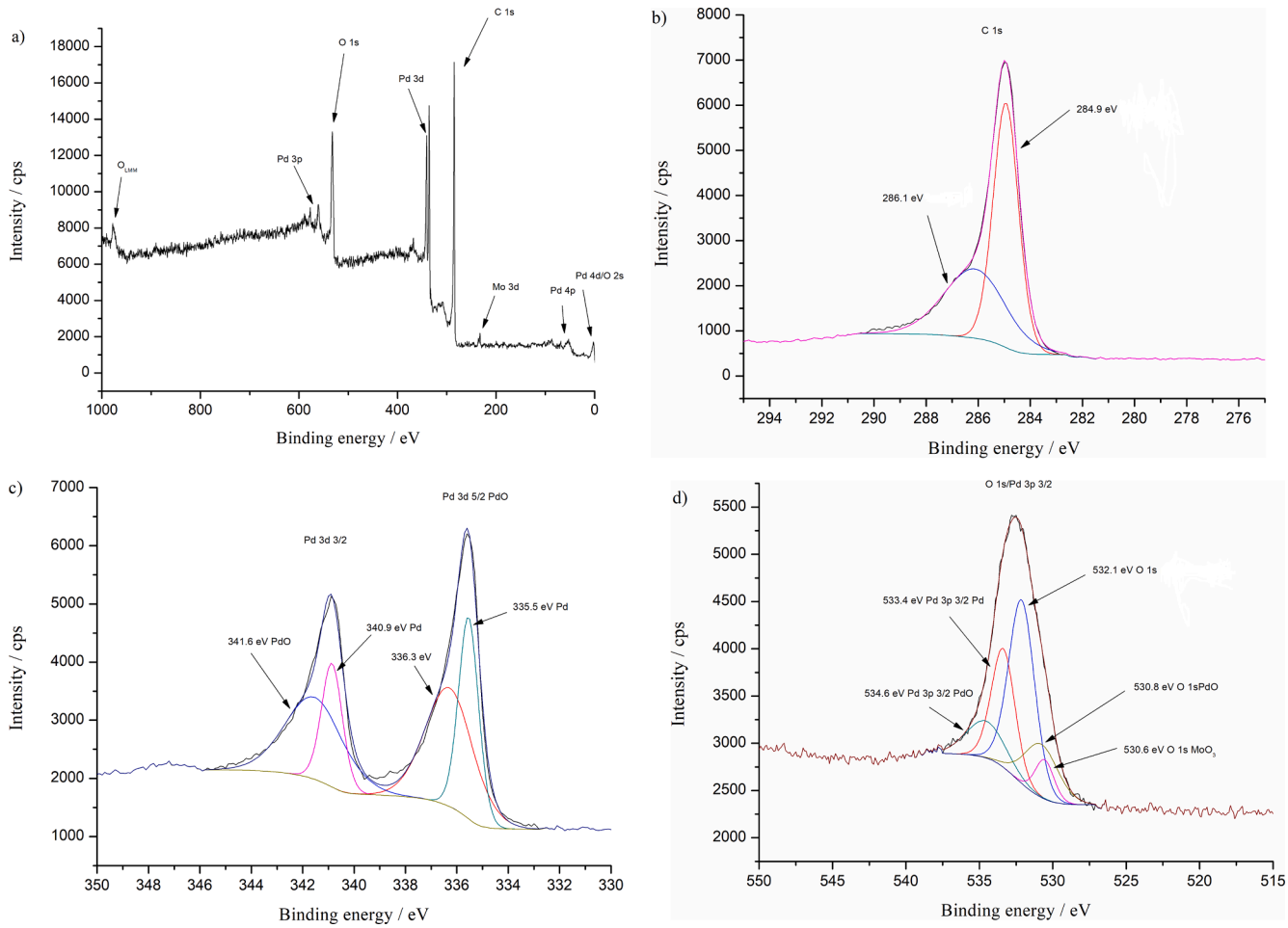

Fig. 3. XPS spectra for Pd@G (a) Survey XPS Spectrum, (b) XPS Spectrum of C 1s, (c) XPS Spectrum of Pd 3d, (d) XPS Spectrum of O 1s Pd 3p.

electrode potential and the equilibrium open-circuit potential ($\eta = E - E_{eq}$; for Pd@G $E_{eq} = -99.6$ mV for $c(H_2O_2) = 5$ mM), a is the intercept ($a = (2.3RT/\alpha nF)\log i_0$), b is the Tafel slope, R is the universal gas constant (8.314 J mol^{-1} K^{-1}), T is the thermodynamic temperature (taken as 295.15 K), α is the electron transfer coefficient, n is the stoichiometric number of electrons in the rate-limiting step, i is the current density, and i_0 is the exchange current density.

As can be seen from Table 1, Pd@G is associated with the smallest Tafel slope of 104.0 mV dec^{-1}, which is significantly lower compared to G (295.8 mV dec^{-1}) and GC electrode (358.4 mV dec^{-1}). Unusual Tafel slopes indicate a significantly high kinetic barrier for the HPRR at G and GC electrodes. In addition, the catalytic activity can be estimated by the exchange current density (i_0) and the onset potential (E_{on}). They were determined from the cathodic Tafel plots (Fig. S1) and cyclic voltammograms, respectively. As implied from i_0 values for Pd@G, the standard rate constant of HPRR appears to be an order of magnitude higher compared to other electrodes, resulting in a significant lowering of the corresponding onset potential (Table 1). Assuming that the reduction mechanism proceeds as a sequential electron transfer process, where the first electron transfer is the rate-limiting step (i.e., $n_\alpha = 1$), the Tafel slope at Pd@G electrode of 104.0 mV yields the electron transfer coefficient value of $\alpha = 0.56$ [6,30]. Also, the product αn_α of the rate-limiting step for Pd@G can be estimated according to Eq. (5) [33], using the cyclic voltammogram recorded at 10 mV s^{-1} (Fig. 5a):

$$\alpha n_\alpha = \frac{47.7 \text{ mV}}{|E_p - E_{\frac{p}{2}}|} \quad (5)$$

where E_p is the peak potential and $E_{p/2}$ is the potential at the half-maximum peak current ($\Delta E = E_p - E_{p/2} = 0.081$ V). The αn_α was calculated to be 0.58, which is almost the same value as the one previously calculated of 0.56 using the Tafel analysis [34].

To further elucidate the electrode mechanisms of H_2O_2 at the Pd@G electrode, the scan rate was varied in the CV in a degassed 0.1 M KOH containing 5 mM H_2O_2 (Fig. 6a). The morphology of the reductive peak strongly depends on the scan rate, transforming from a sharp peak-like shape, typical for the process of an adsorbed reactant ($\nu \leq 20$ mV s^{-1}), to a wave-like shape, associated with a diffusion tale at higher scan rates ($\nu > 20$ mV s^{-1}). Also, contrary to the predictions based on the Randles-Schevcik equation for a simple irreversible process, the peak current decreases by increasing the scan rate from 10 to 50 mV s^{-1}, while the peak potential shifts in a cathodic direction (Fig. 6a). The reduction mechanism at $\nu \leq 20$ mV s^{-1} is controlled by adsorption of the reactant, additionally being gated by a preceding chemical reaction that supplies the electroactive reactant, i.e., a CE mechanism [35]. At $\nu > 50$ mV s^{-1} the peak current is more likely to be affected by the diffusion and electrode kinetics. Thus, at higher scan rates, when the time for the preceding chemical reaction is significantly limited, the direct reduction of H_2O_2 from a dissolved state dominates, which gives rise to the reduction peak at more negative potentials of about −0.350 V (Fig. 6a).

Due to the complexity of the electrode mechanism, neither I_p vs. ν nor I_p vs. $\nu^{1/2}$ is a linear function. The data can be partly explained by studying the ratio $I_p/\nu^{1/2}$ vs. log(ν) (the inset of Fig. 6a), revealing an exponentially decreasing function, which is typical for the CE mechanism, invoking the theoretically predicted dependence of the dimensionless current function on the kinetics of the preceding chemical reaction [35]. The involvement of a preceding chemical reaction in the

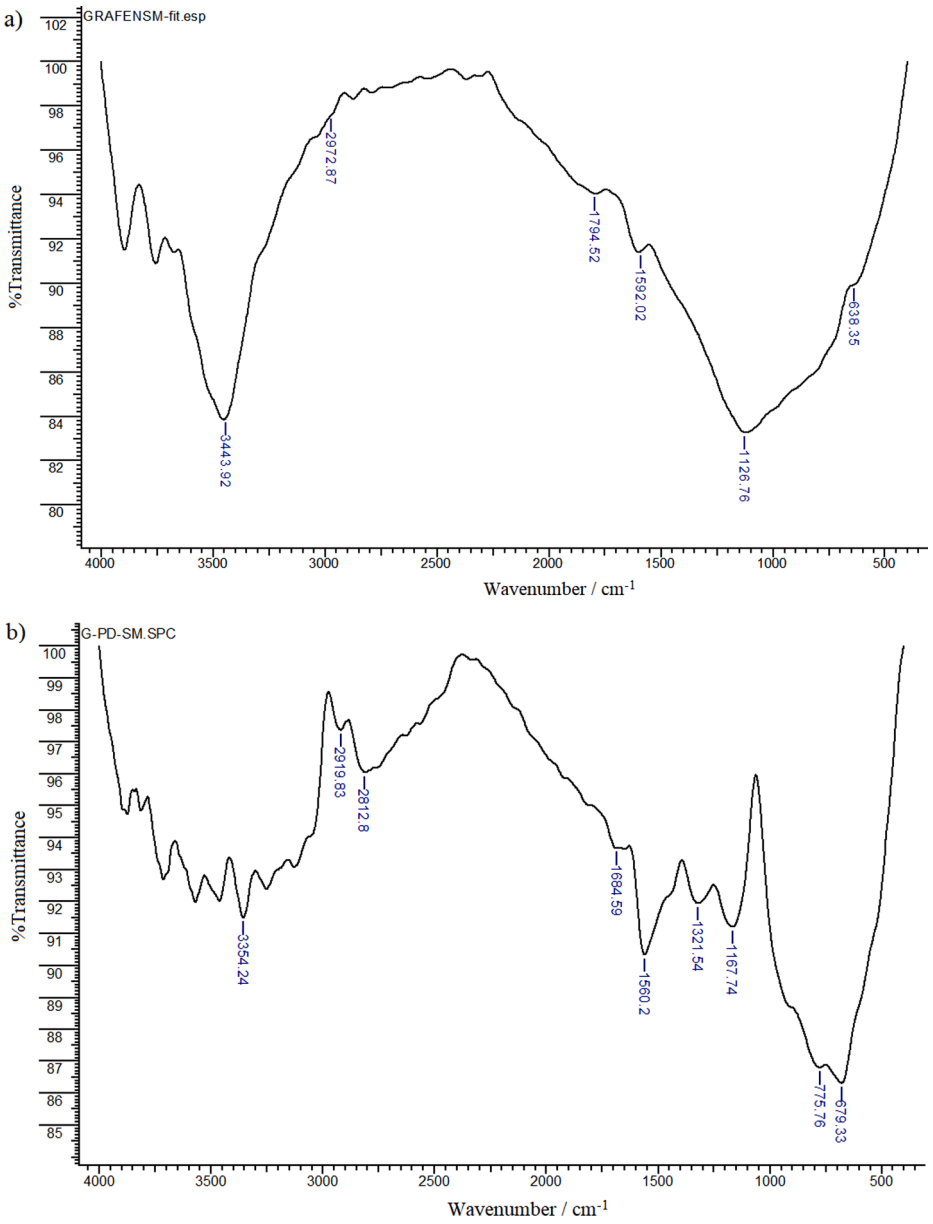

Fig. 4. The FTIR spectra of (a) graphene, (b) Pd@G hybrid in the range of 400–4000 cm^{-1}.

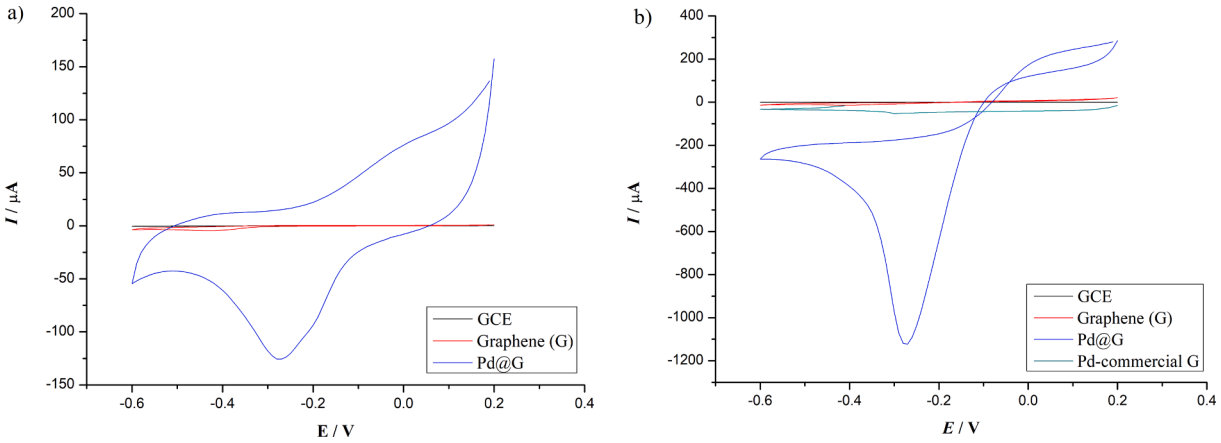

Fig. 5. Cyclic voltammograms recorded at (***a***) GCE, G, and Pd@G in 0.1 M KOH and (***b***) GCE, G, Pd@G, and Pd-commercial G in 0.1 M KOH containing 5 mM H_2O_2. All electrolytes were degassed by purging N_2 before electrochemical measurements. The scan rate was 10 mV s^{-1}.

Table 1
Electrode kinetic parameters were obtained from cyclic voltammetry and Tafel analysis of HPRR for 5 mM H_2O_2 in degassed 0.1 M KOH. Scan rate: 10 mV s^{-1}.

Electrode	E_{on} (mV)	i_0 (μA cm^{-2})	E_{eq} (mV)	$n\alpha$	Tafel slope (mV dec^{-1})	E_p (V)	I_p (μA)
GC	−356	4	−119	0.16	358.4	−0.480	−0.1
G	−152	11.600	−149	0.20	295.8	−0.400	−6.9
Pd@G	−112	123	−100	0.56	104.0	−0.270	−1075

E_{on} – onset potential; i_0 – exchange current density; E_{eq} – equilibrium open-circuit potential; $n\alpha$ – electron transfer number; E_p – peak potential in the CV; I_p – peak current in CV.

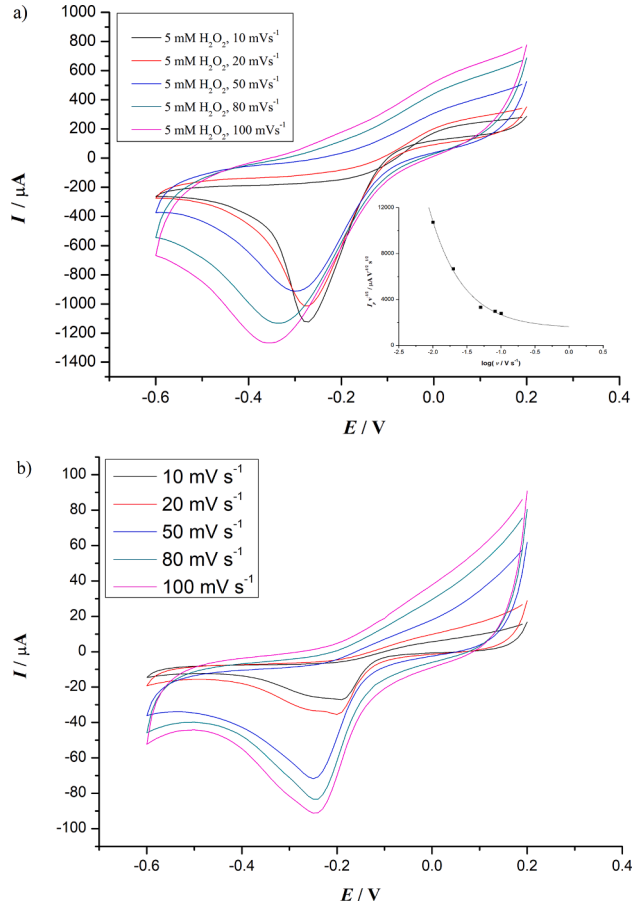

Fig. 6. The scan rate study at Pd@G electrode in 0.1 M KOH (***a***) in the presence of 5 mM H_2O_2 and the absence of O_2 and (***b***) in oxygen saturated solution (P_{O2} = 21 KPa) in the absence of H_2O_2. The inset of panel (***a***) shows the dependency of the scan rate normalized peak current on the logarithm of the scan rate.

electrode mechanism is further supported by the OCP measurements. Specifically, the OCP vale at the Pd@G electrode shifts from −0.985 V to −0.069 V, by increasing the concentration of H_2O_2 gradually from 5 mM to 25 mM. The slope of the linear function E(OCP) vs. log[c(H_2O_2] is close to 50 mV, supporting the assumption that a spontaneous redox transformation of H_2O_2 takes place at the electrode surface.

The scan rate analysis of the oxygen reduction process in the absence of H_2O_2 can partly help in further elucidating the electrode mechanism of H_2O_2 (Fig. 6b). At a low scan rate (v = 10 mV s^{-1}) two reduction processes are obvious, ascribed to the reduction of adsorbed O_2(ads) at about −0.190 V to yield H_2O_2(ads), and further reduction of H_2O_2(ads) at about

−0.270 V. At higher scan rates (v = 100 mV s^{-1}) the reduction peak is associated with a shoulder at potentials more negative than −0.300 V, corresponding to the direct reduction of H_2O_2 from a dissolved state. The function I_p vs. v is less complex compared to the case when H_2O_2 is deliberately added to the electrolyte solution. At $v \leq 50$ mV s^{-1}, the peak current depends linearly on v, implying the adsorption character of the electrode reaction. It is, however, important to stress that the overall voltammetric behaviour does not imply the involvement of a preceding chemical reaction as in the case of the H_2O_2 reduction mechanism.

Considering the sensitivity, the speed of measurements, and the ability for resolution of the voltammetric response, the system was further studied by applying SWV. Fig. 7 compares net SW voltammograms for the reduction of O_2 (curve ***1***), H_2O_2 (curve ***2***), and the mixture of H_2O_2 and O_2 (curve ***3***) at the Pg@G electrode. The SW voltammogram for the reduction of oxygen consists of two well-separated peaks, within the potential interval from −0.200 to −0.300 V, in accord with the cathodic CV peak profile presented in Fig. 5a, thus clearly supporting the two-step reduction mechanism of O_2(ads).

The SW voltammetric profile for H_2O_2 reduction (curve ***2*** in Fig. 7) resembles the profile of the oxygen reduction. The peak current of the main voltammetric peak at about −0.200 V is also affected by the adsorption phenomena, as its intensity reaches saturation for 15 mM H_2O_2. The overall dependence of ⇆ I_p vs. c(H_2O_2) over the concentration interval from 5 to 25 mM obeys a law on an adsorption isotherm (data not shown), suggesting the electrode mechanism proceeds from an adsorbed state of the reactant, similar as in the case of oxygen reduction. Moreover, the half-peak width of the main peak for H_2O_2 reduction located at −0.200 V is 152 mV (curve ***2*** in Fig. 7), being very close to the half-peak with of the overall voltammetric profile of the oxygen reduction which is 162 mV (curve ***1*** in Fig. 7).

However, the voltammetric behaviour of O_2 and H_2O_2 reduction upon variation of the frequency is significantly different. The main peak of H_2O_2 reduction is located at about −0.200 V, the increase of the frequency from 1 to 12.5 Hz (i.e., shortening the duration of potential pulses) causes the peak current to decrease. The frequency-normalized

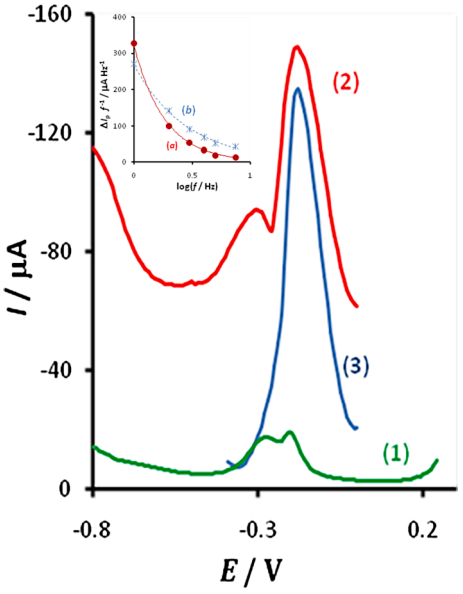

Fig. 7. Typical net square wave voltammograms at Pd@G electrode in 0.1 M KOH for the reduction of oxygen (1), hydrogen peroxide (2), and the mixture of hydrogen peroxide and oxygen (3). The concentration of H_2O_2 is 5 mM H_2O_2 for (2) and (3), while the solution was air saturated for (1) and (3). The parameters of the SWV are SW frequency 2 Hz, amplitude 10 mV, and the step potential 10 mV. The inset shows the dependence of the frequency normalized net peak current (ΔIp/f) as a function of the logarithm of the frequency for H_2O_2 corresponding to the main peak at −0.200 V (curve ***a***) and for the mixture of H_2O_2 and O_2 (curve ***b***).

net peak current ⇆ I_p/f decreases with the logarithm of the frequency, as typical for the CE mechanisms [36] (the inset of Fig. 7, curve (***a***)), supporting the data obtained with cyclic voltammetry (the inset of Fig. 6a). Noteworthy, in the case of oxygen reduction, the intensity of the overall response is a linear function of the frequency, confirming the adsorption character of the two electrode reactions represented by the split net SW peak (curve ***1*** in Fig. 7), without the involvement of a preceding chemical reaction. Also, the second reduction peak of H_2O_2, located at more negative potentials of −0.300 V (curve ***2*** in Fig. 7) has a more pronounced diffusion character, being significantly different compared to the voltammetric features of the electrode process at −0.200 V. Thus, it is associated with the electrode reaction proceeding from a dissolved state of the reactant, which corresponds to the electrode process discussed in the context of Fig. 6a, observed at scan rates $v > 50$ mV s^{-1}.

It is finally highly intriguing to analyze the voltammetric profile obtained in the presence of both oxygen and hydrogen peroxide in the solution (curve ***3*** in Fig. 7). The electrode mechanism is characterized by distinct features. It is a sharp peak with a peak width significantly smaller than the main peak for H_2O_2 reduction (compare curve ***3*** and the main peak of curve ***2***). The electrode process proceeding from the dissolved state of H_2O_2 (i.e., the SW peak at −0.330 V in curve ***2***, Fig. 7) is completely absent in the mixture of H_2O_2 and O_2 in the solution. The half-peak width of curve ***3*** (120 mV) coincides with the half-peak width of the first SW peak (128 mV) for the oxygen reduction, located at −0.210 V (curve ***1*** in Fig. 7). The half-peak width of the latter peak was obtained by deconvolution of the voltammetric profile for oxygen reduction (curve ***1*** in Fig. 7). Moreover, the intensity of the voltammetric peak in the presence of both H_2O_2 and O_2 ($\Delta I_p = 121$ μA) exceeds the sum of the responses of O_2 ($\Delta I_p = 15.5$ μA) and H_2O_2 ($\Delta I_p = 86.3$ μA), implying an additional catalytic effect. Importantly, the overall catalytic effect is not manifested by decreasing the overpotential (i.e., an increase of the standard rate constant of a particular electrode reaction), rather than it implies the enhancement of the current due to resupply of the electroactive material, as typical for the EC', regenerative catalytic mechanism [37]. The dependence of the frequency-normalized net peak current ($\Delta I_p/f$) vs. log(f) is different compared to the reduction of H_2O_2 in the absence of O_2 (compare curves ***a*** and ***b*** in the inset of Fig. 7), though both reaction mechanisms are affected by a coupled chemical reaction.

4. Discussion

4.1. XRD

A sharp peak at around 26.3° is assigned to the (0 0 2) crystallographic plane of graphene nanoparticles composed mainly of the stacked graphene sheets up to a few layers (Fig. 1) [13]. The corresponding d-spacing (the distance between the graphene layers) of 0.338 nm was found using Bragg's equation (Eq. (6)). This value matches the value found in the literature [38].

$$2d\sin\theta = n\lambda \tag{6}$$

After Pd deposition onto graphene under hydrothermal conditions, the (0 0 2) peak was observed at the same 2-theta value (Fig. 1b), indicating that Pd nanoparticles, water molecules, and oxygen functionalities have not been incorporated between the layers.

Four reflections observed in Fig. 1b at around 2-theta angles of 40.2°, 46.8°, 68.1° and 82.3° are ascribed to Pd (1 1 1), (2 0 0), (2 2 0), and (3 1 1) crystal planes of a face-centered cubic (fcc) structure of palladium (JCPDS-ICDD, Card No. 04-802), respectively. The interplanar spacing for (1 1 1) and (2 0 0) lattice planes of the face-centered cubic (fcc) structure of Pd was 0.224 nm and 0.194 nm, respectively.

The lattice parameter (αPd) values of the metal particles were obtained using the Pd (2 2 0) diffraction peak of the prepared Pd@G hybrid. The lattice constant value of dispersed Pd nanoclusters was calculated to be 3.891 Å using Eq. (7), which is the same value as 3.890 Å for pure Pd [39].

$$\sin(\theta) = \frac{\lambda\sqrt{h^2 + k^2 + l^2}}{2a} \tag{7}$$

Furthermore, the average crystallite sizes of palladium particles have been obtained at 13 nm using the Debye Scherrer equation (Eq. (8)). Thus, the presence of palladium NPs increases the electrocatalytic activity of the nanohybrid.

$$D = K\lambda/(\beta\cos\theta) \tag{8}$$

$$\lambda = 0.154\,\text{nm} \tag{9}$$

where $K = 0.89$ is a constant related to the crystallite shape, the X-ray wavelength is $\lambda = 0.154$ nm, the FWHM value of Pd (2 2 0) diffraction peak shown by β, and θ is the diffraction angle. The activity of the Pd-based electrocatalyst was mainly associated with an optimum Pd lattice strain. The Pd lattice strain, ε, was calculated from the peak positioned at $2\theta \approx 68.1°$, which is ascribed to the (2 2 0) reflection of the Pd fcc crystal structure, using the equation [7,40]:

$$\varepsilon\ (\%) = \frac{\beta_{hkl}}{4\tan\theta}100 \tag{10}$$

The calculated lattice strain value is 0.42%. Bampos et al. [7] reported that optimal strain values for Pd electrocatalyst are between 0.4 and 0.6%. The crystallite size for bare graphene powder was found to be 9.33 nm and 11.23 nm after Pd deposition under HT conditions, which is comparable with the reported value [7].

4.2. Morphological characterization and EDX

The SEM images showed that the as-prepared graphene (Fig. 2a) has a sheet morphology composed of layers with different orientations, which provides more exposed active sites for Pd nucleation. The graphene retained the same morphology after deposition of Pd nanoparticles (Pd@G sample in Fig. 2b).

Iron and chlorine are present in both G and Pd@G samples, as indicated by EDX spectra shown in Fig. 2c–d. Their presence can be ascribed to the synthesis procedure which includes the addition of $FeCl_3$ and treatment with HCl in the final step. Fig. 2f provides evidence for homogeneous dispersion of Pd metallic NPs all over the graphene surface, which increases the electrocatalytic activity of the electrode.

The EDX analysis indicated that the G consisted of 91.98 wt% C, 0.97 wt% Fe, and 3.56 wt% O, while Pd@G contains 61.89 wt% C, 25.08 wt% Pd, 0.88 wt% Fe, and 10.6 wt% O.

4.3. XPS

As can be seen in the XPS spectrum of C 1s (Fig. 3b), the peak located around 284.9 eV with a shoulder at 287 eV can be deconvoluted into two peaks at 284.9 and 286.1 eV were assigned to C—C(sp2C) and C—O groups, respectively [41].

The XPS spectrum of Pd 3d (Fig. 3c) presents a core level doublet (Pd3d5/2 and Pd3d3/2). The Pd3d5/2 can be deconvoluted into two peaks, which demonstrates the presence of two formats of Pd. As can be seen, the two peaks at 336.3 eV and 335.5 eV were attributed to the bonding energy of Pd (II) and metallic Pd, respectively. The Pd3d3/2 peak can be also divided into two peaks at 341.6 eV and 340.9 eV which were assigned to Pd (II) and metallic Pd, respectively [42–44]. The Pd (II) peaks may be caused by the surface oxidation and/or chemisorption of oxygen during the preparation process.

The deconvoluted XPS spectrum of O 1s Pd 3p (Fig. 3d) shows the intense peak at a binding energy of 532.1 eV which was associated with adsorbed oxygen, then two peaks located at 530.8 and 530.6 eV inherent O atoms bound to metals [45]. Also, there are two peaks at 534.6 and

533.4 eV assigned to the binding energy of Pd 3p 3/2 PdO and Pd 3p 3/2 Pd, respectively [46].

4.4. FTIR spectroscopy

The FTIR spectra of graphene (G) and Pd@G nanocomposite are shown in Fig. 4. According to the literature, there are several characteristic peaks in the absorption bands of the spectra. Fig. 4a represents the FTIR spectrum of synthesized graphene in the range of 400–4000 cm^{-1}. The six peaks of graphene in FTIR spectrum are located at 3443.92 cm^{-1}, 2972.87 cm^{-1}, 1794.52 cm^{-1}, 1592.02 cm^{-1}, 1126.76 cm^{-1}, and 638.35 cm^{-1}. The peak at 3443.92 cm^{-1} is attributed to the stretching vibration of the hydroxyl group [47]. The peaks at 2972.87 cm^{-1} and 1794.52 cm^{-1} are attributed to the C—H bond stretching vibration, and C═O stretching, respectively [48]. The peaks of graphene at 1592.02 cm^{-1}, 1126.76 cm^{-1}, and 638.35 cm^{-1} confirm the existence of C═C stretching, C—O stretching vibration, and C═C bending vibration, respectively [44,49].

Fig. 4b represents the FTIR spectrum of Pd@G nanocomposite in the range of 400–4000 cm^{-1}. Due to the reduction of graphene surface groups by NaBH4 during the synthesis procedure, most of the absorption bands in the FTIR spectrum of Pd@G are shifted, decreased in intensity, or removed than those in the FTIR spectrum of graphene. For example, the band corresponding to the stretching vibration of the hydroxyl group is of lower intensity and appears at 3354.24 cm^{-1} [47]. The bands at 2919.83 cm^{-1} and 2812.8 cm^{-1} attributed to the C—H bond stretching vibration are of higher intensity, compared to the C—H bond stretching vibration band in the spectrum of graphene. While bands at 1684.59 cm^{-1} and 1560.2 cm^{-1} are assigned to the C═C stretching [44,49–51]. The peaks at 1321.54 cm^{-1} and 1167.74 cm^{-1} confirm the existence of C—O stretching vibration [44,49]. Finally, the peaks at 775.76 cm^{-1} and 679.33 cm^{-1} are attributed to the vibrations of the C—H bonds of the benzene rings [49–50].

4.5. HPRR (hydrogen peroxide reduction reaction)

Comparing voltammetric characteristics of GCE, G, Pd-commercial G, and Pg@G electrodes one concludes clearly that the Pd@G electrode exhibits superior electrocatalytic activity toward HPRR. The most striking feature at the Pd@G electrode is the disproportionation reaction of H_2O_2 proceeding as a surface process of adsorbed species at the Pd@G hybrid (Eq. (11)) [30,52–54]:

$$2HO_2^-(ads) = O_2(ads) + 2HO^-(ads) \quad (11)$$

The extent and kinetics of reaction (11) depend markedly on the concentration of both H_2O_2 and O_2 in the electrolyte solution. Another important fact of general importance for elucidation of the overall electrode mechanism is the strong and competitive adsorption of O_2 and its catalytic reduction via the two-step surface mechanism (i.e., surface EE mechanism) described by Eqs. (12) and (13):

$$O_2(ads) + 2H_2O + 2e^- = H_2O_2(ads) + 2OH^-(ads) \quad (12)$$

$$H_2O_2(ads) + 2e^- = 2OH^-(ads) \quad (13)$$

which correspond to the voltammetric profiles in Figs. 5a, 6b, and 7 (curve ***1***).

The extent of reaction (11) is less significant for the EE reduction mechanism of O_2(ads) in the absence of H_2O_2 in the electrolyte solution, as electrochemically formed H_2O_2(ads) is exhausted by the electrochemical reaction (13) at potentials of about −0.270 V (Figs. 5a and 6b), being very close to the potential of the reaction (12). Moreover, the excess of O_2 in the solution disfavours the extent of reaction (11) and shifts the chemical equilibrium toward the left-hand side.

When H_2O_2 is deliberately added into the electrolyte solution in the absence of dissolved oxygen, reaction (11) is of critical importance, producing adsorbed oxygen as an electrochemical reactant before the voltammetric scan is applied. In addition, the same reaction proceeds in the course of the voltammetric scan as soon as the adsorbed oxygen is electrochemically exhausted. Consequently, the electrochemical reduction of O_2(ads) generated by the disproportionation of H_2O_2(ads) proceeds according to a CE reaction scheme [35–36], where the C step is represented by reaction (11) and the E step is a reaction (12), which is supported by the voltammetric behaviour under varying scan rate in CV (Fig. 6a) and the frequency analysis in SWV (the inset of Fig. 7, curve ***a***). The CE reaction scheme is followed by an additional electrode reaction (13), i.e., further reduction of electrochemically formed H_2O_2(ads). However, in a large excess of H_2O_2 in the electrolyte solution reaction (13) proceeds independently as well, as H_2O_2(ads) coexists in equilibrium with O_2(ads) on the electrode surface. For these reasons, the reduction mechanism of H_2O_2 in the absence of dissolved oxygen is manifested as a single reduction peak in CV, extended over the potential region from −0.200 to −0.300 V (Fig. 5b), and a single SW voltammetric peak (Fig. 7, the main peak of curve ***2***) with a half-peak width almost identical to the overall half-peak width of the curve ***1*** in Fig. 7. The overall electrochemical mechanism exhibits very complex voltammetric behaviour, being strongly dependent on the time of the experiment reflecting the adsorption character of the electrode processes and the strong influence of the chemical reaction (11), and the sequential character of the overall electron transfer mechanism represented by two-electrode reactions (12) and (13), which are merged in a single voltammetric peak (e.g., Fig. 5b and the main peak of curve ***2*** in Fig. 7). Moreover, in a large excess of H_2O_2, the reduction process from a dissolved state of H_2O_2 takes place at potentials more negative than −0.300 V, manifested as a small, second peak in the SW voltammogram (curve ***2*** in Fig. 7). It is a sluggish diffusion affected electrode process, which emerges under conditions of CV at higher scan rates (Fig. 6a, $\nu \geq$ 50 mV s^{-1}), or as a shoulder of the voltammetric profiles in Fig. 6b at $\nu \geq$ 80 mV s^{-1}.

The reaction scenario for the H_2O_2 reduction significantly changes in a solution saturated with oxygen, as clearly evidenced by SW voltammetric data (curve ***3*** and the inset of Fig. 7). Under such conditions, the overall voltammetric behaviour suggests an EC' reaction scheme (i.e., a regenerative catalytic mechanism) [37], based predominantly on the first electrode reaction (12). The strong and competitive adsorption of dissolved oxygen occupies predominantly the adsorption sites on the electrode surface, precluding reaction (11) to proceed at a significant degree before the voltammetric scan. Thus, the electrode mechanism commences with the reduction of O_2(ads) (Eq. (12)), which generates adsorbed H_2O_2. However, as the concentration of H_2O_2 in the diffusion layer is large, being almost identical as in the bulk of the solution, reaction (11) proceeds at a significant rate in the course of the voltammetric pulses, resupplying the adsorbed oxygen on the electrode surface. Thus, electrode reaction (12), followed by the surface redox reaction (11), completes a CE' reaction scheme, resulting in a distinct peak-current-frequency dependence (see the inset of Fig. 7). The voltammetric peak (curve ***3*** in Fig. 7) is located at potentials typical for the electrode reaction (12), with a peak-current determined by the kinetics of the reaction (12) augmented by the kinetics of reaction (11). Also, the half-peak width of curve ***3*** is significantly smaller compared to both curves ***2*** and ***1*** in Fig. 7, implying that the contribution of the electrode reaction (13) is insignificant in the overall voltammetric profile. Intriguingly, oxygen plays the role of a redox mediator for the reduction of H_2O_2 at the Pd@G electrode, clearly revealing that future analytical application of this profound electrocatalyst for detection of H_2O_2 should be applied in oxygen saturated solutions.

5. Conclusions

Pd@C hybrid material was successfully synthesized by a simple hydrothermal method and used as an electrocatalyst for HPRR. X-ray diffraction confirmed the presence of peaks assigned to the

crystallographic planes of graphene and immobilized Pd particles. Elemental mapping showed uniform and catalytically favourable dispersion of Pd all over the graphene surface, while the SEM image showed a layered structure of the hybrid.

The Pd@C hybrid material exhibits a significant electrocatalytic effect toward electrochemical reduction of H_2O_2 compared to the bare and graphene modified glassy carbon electrode in alkaline conditions. The electrocatalytic mechanism is predominantly controlled by the strong adsorption of both hydrogen peroxide and oxygen on palladium nanoparticles and the disproportionation reaction of adsorbed H_2O_2, undergoing a heterogeneous redox reaction on the surface of palladium nanoparticles. Traces of adsorbed oxygen exist on the surface of palladium nanoparticles even in the absence of dissolved oxygen in the electrolyte solution, whereas in the presence of H_2O_2 in the solution, both H_2O_2(ads) and O_2(ads) coexist on the electrode surface, the latter being formed mainly by the disproportionation of H_2O_2(ads). Thus, the electrode mechanism involves the reduction of O_2(ads), as a slightly more favoured electrode process, followed by the reduction of H_2O_2(ads). The two electrode reactions (12) and (13) are manifested mainly as a single voltammetric peak in the presence of H_2O_2 in the solution. Both electrode reactions are two-electron transfer processes, most probably kinetically limited by the first electron transfer. However, under dynamic conditions of the voltammetric experiment, electrode reactions (12) and (13) are strongly intertwined. Rigorously speaking, the reduction of O_2(ads), previously formed by the disproportionation reaction of H_2O_2(ads), is not a conventional CE mechanism, rather than it is a catalytic mechanism of the second kind, theoretically studied in our previous work [55], where the initial reactant (i.e., H_2O_2) generates an electroactive reactant (i.e., O_2) through a chemical reaction, whereas the product of the electrode reaction (i.e., reduction of O_2) regenerates the initial reactant (i.e., H_2O_2). The second electrode reaction (i.e., electrode reduction of H_2O_2(ads), Eq. (13)) is also very complex, as it is affected by the adsorption equilibrium of H_2O_2, disproportionation reaction (11) which exhausts H_2O_2(ads), and the electrode reaction (12), which electrochemically generates H_2O_2(ads).

Finally, in an oxygen saturated electrolyte solution containing H_2O_2, the electrode mechanism simplifies while the catalytic effect enhances. The main reason is the dominant adsorption of oxygen, which precludes the hydrogen peroxide adsorption; thus, the disproportionation reaction is insignificant prior to the electrochemical reduction of O_2(ads). In the course of the electrode reaction (12), the electrochemical reactant O_2(ads) is resupplied by the follow-up redox reaction (i.e., disproportionation reaction (11)), thus completing an EC reaction mechanism of an adsorbed reactant, as theoretically outlined in our previous study [56]. Under such conditions the fast kinetics of the disproportionation reaction exhausts the surface concentration of H_2O_2(ads), thus precluding the second electrode reaction of the direct reduction of H_2O_2(ads). Moreover, the adsorption equilibrium of O_2 also supports additional O_2(ads) on the electrode surface, which all together results in a strong electrocatalytic catalytic effect, providing a basis for future analytical application of the studied mechanism for H_2O_2 determination.

CRediT authorship contribution statement

Jelena Čović: Investigation, Visualization, Writing – original draft. **Valentin Mirceski:** Visualization, Writing – review & editing. **Aleksandra Zarubica:** Writing – review & editing. **Dirk Enke:** Formal analysis. **Simon Carstens:** Formal analysis. **Aleksandar Bojić:** Writing – review & editing, Funding acquisition. **Marjan Ranđelović:** Conceptualization, Writing – review & editing, Supervision.

Declaration of Competing Interest

The authors declare that they have no known competing financial interests or personal relationships that could have appeared to influence the work reported in this paper.

Acknowledgments

The authors would like to acknowledge financial support from the Ministry of Education, Science and Technological Development of the Republic of Serbia (Agreement No 451-03-68/2020-14/200124). V. M. acknowledges the support by the NATO Science for Peace and Security Programme (grant SPS G5550).

Appendix A. Supplementary material

Supplementary data to this article can be found online at https://doi.org/10.1016/j.apsusc.2021.151633.

References

[1] W. Chen, S. Cai, Q.-Q. Ren, W. Wen, Y.-D. Zhao, Recent advances in electrochemical sensing for hydrogen peroxide: a review, Analyst 137 (2012) 49, https://doi.org/10.1039/C1AN15738H.
[2] E.J. Calvo, D.J. Schiffrin, The reduction of hydrogen peroxide on passive iron in alkaline solutions, J. Electroanal. Chem. 163 (1984) 257–275, https://doi.org/10.1016/S0022-0728(84)80056-X.
[3] O. Špalek, J. Balej, I. Paseka, Kinetics of the Decomposition of Hydrogen Peroxide in Alkaline Solutions, J. Chem. Soc., Faraday Trans. I 78 (1982) 2349–2359, https://doi.org/10.1039/F19827802349.
[4] T. Poux, A. Bonnefont, A. Ryabova, G. Kéranguéven, G.A. Tsirlina, E.R. Savinova, Electrocatalysis of hydrogen peroxide reactions on perovskite oxides: experiment versus kinetic modeling, Phys. Chem. Chem. Phys. 16 (2014) 13595–13600, https://doi.org/10.1039/C4CP00341A.
[5] T.C. Nagaiah, D. Schäfer, W. Schuhmann, N. Dimcheva, Electrochemically Deposited Pd−Pt and Pd−Au Codeposits on Graphite Electrodes for Electrocatalytic H_2O_2 Reduction, Anal. Chem. 85 (2013) 7897–7903, https://doi.org/10.1021/ac401317y.
[6] S.J. Amirfakhri, J.-L. Meunier, D. Berk, Electrocatalytic activity of $LaNiO_3$ toward H_2O_2 reduction reaction: Minimization of oxygen evolution, J. Power Sources 272 (2014) 248–258, https://doi.org/10.1016/j.jpowsour.2014.08.068.
[7] G. Bampos, L. Sygellou, S. Bebelis, Oxygen reduction reaction activity of Pd-based bimetallic electrocatalysts in alkaline medium, Catal. Today 355 (2020) 685–697, https://doi.org/10.1016/j.cattod.2019.06.010.
[8] W.J. Work, K. Horie, M. Hess, R.F.T. Stepto, Definitions of terms related to polymer blends, composites, and multiphase polymeric materials (IUPAC Recommendations, Pure Appl Chem. 76 (2004) (2004) 1985–2007, https://doi.org/10.1351/pac200476111985.
[9] P. Płócienniczak, T. Rębiś, M. Nowicki, G. Milczarek, A green approach for hybrid material preparation based on carbon nanotubes/lignosulfonate decorated with silver nanostructures for electrocatalytic sensing of H_2O_2, J. Electroanal. Chem. 880 (2021), https://doi.org/10.1016/j.jelechem.2020.114896.
[10] S. Li, X. Zhanga, H. Chena, H. Hua, J. Liua, Y. Zhanga, Y. Pana, Y. Zheng, Electrocatalytic effect of 3D porous sulfur/gallium hybrid materials in lithium–sulfur batteries, Electrochim. Acta 364 (2020), https://doi.org/10.1016/j.electacta.2020.137259.
[11] J. Li, W. Yang, H. Zhu, X. Wang, F. Yang, B. Zhang, X. Yang, In situ PEI and formic acid directed formation of Pt NPs/MWNTs hybrid material with excellent electrocatalytic activity, Talanta 79 (2009) 935–939, https://doi.org/10.1016/j.talanta.2009.05.029.
[12] M.U.A. Prathap, V. Anuraj, B. Satpati, R. Srivastava, Facile preparation of Ni $(OH)_2$–MnO_2 hybrid material and its application in the electrocatalytic oxidation of hydrazine, J. Hazard. Mater. 262 (2013) 766–774, https://doi.org/10.1016/j.jhazmat.2013.09.050.
[13] B. Rajesh, K.R. Thampi, J.-M. Bonard, H.J. Mathieu, N. Xanthopoulos, B. Viswanathan, Electronically conducting hybrid material as high performance catalyst support for electrocatalytic application, J. Power Sources 141 (2005) 35–38, https://doi.org/10.1016/j.jpowsour.2004.09.014.
[14] N. Li, M. Zhu, M. Qu, X. Gao, X. Li, W. Zhang, J. Zhang, YeIron-tetrasulfophthalocyanine functionalized graphene nanosheets: Attractive hybrid nanomaterials for electrocatalysis and electroanalysis, J. Electroanal. Chem. 651 (2011) 12–18, https://doi.org/10.1016/j.jelechem.2010.11.012.
[15] Y. Wang, Y. Rui, F. Li, M. Li, Electrodeposition of nickel hexacyanoferrate/layered double hydroxide hybrid film on the gold electrode and its application in the electroanalysis of ascorbic acid, Electrochim. Acta 117 (2014) 398–404, https://doi.org/10.1016/j.electacta.2013.11.141.
[16] R. Yan, K. Wang, C. Wang, H. Zhang, Y. Song, Q. Guo, J. Wang, Synthesis and in-situ functionalization of graphene films through graphite charging in aqueous $Fe_2(SO_4)_3$, Carbon 107 (2016) 379–387, https://doi.org/10.1016/j.carbon.2016.06.018.
[17] L. Li, M. Wang, M. Cao, H. Qiu, Z. Yang, L. Xu, J. Li, Regulation of radicals from electrochemical exfoliation for production of graphene and its electrochemical properties, Electrochim. Acta 258 (2017) 1484–1492, https://doi.org/10.1016/j.electacta.2017.12.021.

[18] Y. Zhang, Y. Xu, Simultaneous Electrochemical Dual-Electrode Exfoliation of Graphite toward Scalable Production of High-Quality Graphene, Adv. Funct. Mater. 29 (2019) 1902171, https://doi.org/10.1002/adfm.201902171.

[19] L. Li, M. Wang, J. Guo, M. Cao, H. Qiu, L. Dai, Z. Yang, Regulation of radicals from electrochemical exfoliation of a double-graphite electrode to fabricate high-quality graphene, J. Mater. Chem. C 6 (2018) 6257–6263, https://doi.org/10.1039/C8TC01565A.

[20] M. Guler, V. Turkoglu, A. Kivrak, F. Karahan, A novel nonenzymatic hydrogen peroxide amperometric sensor based on Pd@CeO_2-NH_2 nanocomposites modified glassy carbon electrode, Mat. Sci. Eng. C 90 (2018) 454–460, https://doi.org/10.1016/j.msec.2018.04.084.

[21] S. Li, S. Ma, Y. Zhang, L. Zhao, H. Yang, R. Jin, Metal-organic interface engineering for coupling palladium nanocrystals over functionalized graphene as an advanced electrocatalyst of methanol and ethanol oxidation, J. Colloid Interf. Sci. 588 (2021) 384–392, https://doi.org/10.1016/j.jcis.2020.12.080.

[22] S. Li, J. Shu, S. Ma, H. Yang, J. Jin, X. Zhang, R. Jin, Engineering three-dimensional nitrogen-doped carbon black embedding nitrogen-doped graphene anchoring ultrafine surface-clean Pd nanoparticles as efficient ethanol oxidation electrocatalyst, Appl. Catal. B-Environ. 280 (2021), https://doi.org/10.1016/j.apcatb.2020.119464.

[23] C. Xu, L. Zhang, L. Liu, Y. Shi, H. Wang, X. Wang, F. Wang, B. Yuan, D. Zhang, A novel enzyme-free hydrogen peroxide sensor based on polyethylenimine-grafted graphene oxide-Pd particles modified electrode, J. Electroanal. Chem. 731 (2014) 67–71, https://doi.org/10.1016/j.jelechem.2014.08.003.

[24] M. Guler, V. Turkoglu, A. Bulut, M. Zahmakiran, Electrochemical sensing of hydrogen peroxide using Pd@Ag bimetallic nanoparticles decorated functionalized reduced graphene oxide, Electrochim. Acta 263 (2018) 118–126, https://doi.org/10.1016/j.electacta.2018.01.048.

[25] S. Bozkurt, B. Tosun, B. Sen, S. Akocak, A. Savk, M.F. Ebeoğlugil, F. Sen, A hydrogen peroxide sensor based on TNM functionalized reduced graphene oxide grafted with highly monodisperse Pd nanoparticles, Anal. Chim. Acta 989 (2017) 88–94, https://doi.org/10.1016/j.aca.2017.07.051.

[26] M. Guler, Y. Dilmac, Palladium nanoparticles decorated (3-aminopropyl) triethoxysilane functionalized reduced graphene oxide for electrochemical determination of glucose and hydrogen peroxide, J. Electroanal. Chem. 834 (2019) 49–55, https://doi.org/10.1016/j.jelechem.2018.12.052.

[27] B. Zhang, J. Song, G. Yang, B. Han, Large-scale production of high-quality graphene using glucose and ferric chloride, Chem. Sci 5 (2014) 4656–4660, https://doi.org/10.1039/C4SC01950D.

[28] S.V. Sokolov, L. Sepunaru, R.G. Compton, Taking cues from nature: Hemoglobin catalysed oxygen reduction, Appl. Mat. Today 7 (2017) 82–90, https://doi.org/10.1016/j.apmt.2017.01.005.

[29] S.J. Percival, J.E. Dick, A.J. Bard, Cathodically Dissolved Platinum Resulting from the O_2 and H_2O_2 Reduction Reactions on Platinum Ultramicroelectrodes, Anal. Chem. 89 (2017) 3087–3092, https://doi.org/10.1021/acs.analchem.6b04832.

[30] X. Cai, E.E.L. Tanner, C. Lin, K. Ngamchuea, J.S. Foord, R.G. Compton, The Mechanism of Electrochemical Reduction of Hydrogen Peroxide on Silver Nanoparticles, Phys. Chem. Chem. Phys. 20 (2017) 1608–1614, https://doi.org/10.1039/C7CP07492A.

[31] M.P. Marceta Kaninski, D.P. Saponjic, I.M. Perovic, A.D. Maksic, V.M. Nikolic, Electrochemical characterization of the Ni–W catalyst formed in situ during alkaline electrolytic hydrogen production—Part II, Appl. Catal. A: Gen. 405 (2011) 29–35, https://doi.org/10.1016/j.apcata.2011.07.015.

[32] Fritz Scholz, Electroanalytical Methods, Guide to Experiments and Applications Second, Revised and Extended Edition, Springer Heidelberg Dordrecht London New York, 2010. DOI: 10.1007/978-3-642-02915-8.

[33] R. Liu, Y. Wei, Y. Zheng, H. Zhang, Q. Sheng, A hydrogen peroxide sensor based on silver nanoparticles biosynthesized by Bacillus subtilis, Chin. J. Chem. 31 (2013) 1519–1525, https://doi.org/10.1002/cjoc.201300487.

[34] Y. Zhang, C. Zhang, D. Zhang, M. Ma, W. Wang, Q. Chen, Nano-assemblies consisting of Pd/Pt nanodendrites and poly (diallyldimethylammonium chloride)-coated reduced graphene oxide on glassy carbon electrode for hydrogen peroxide sensors, Mat. Sci. Eng. C 58 (2016) 1246–1254, https://doi.org/10.1016/j.msec.2015.09.015.

[35] R.G. Compton, C.E. Banks, Understanding Voltammetry Third Edition, World Scientific Publishing Europe Ltd., London, 2018. ISBN 9781786345295.

[36] D. Guziejewski, Electrode mechanisms with coupled chemical reaction — Amplitude effect in square-wave voltammetry, J. Electroanal. Chem. 870 (2020), https://doi.org/10.1016/j.jelechem.2020.114186.

[37] R. Gulaboski, V. Mirceski, New aspects of the electrochemical-catalytic (EC') mechanism in square-wave voltammetry, Electrochim. Acta 167 (2015) 219–225, https://doi.org/10.1016/j.electacta.2015.03.175.

[38] A.A. Khodiri, M.Y. Al-Ashry, A.G. El-Shamy, Novel hybrid nanocomposites based on polyvinyl alcohol/graphene/magnetite nanoparticles for high electromagnetic shieldingperformance, J. Alloys Compd. 847 (2020), https://doi.org/10.1016/j.jallcom.2020.156430.

[39] B. Şen, A. Aygün, T.O. Okyay, A. Şavk, R. Kartop, F. Şen, Monodisperse palladium nanoparticles assembled on graphene oxide with the high catalytic activity and reusability in the dehydrogenation of dimethylamine-borane, Int. J. Hydrogen Energy 43 (2018) 20176–20182, https://doi.org/10.1016/j.ijhydene.2018.03.175.

[40] V.D. Mote, Y. Purushotham, B.N. Dole, Williamson-Hall analysis in estimation of lattice strain in nanometer-sized ZnO particles, J. Theor. Appl. Phys. 6 (2012) 1–8, https://doi.org/10.1186/2251-7235-6-6.

[41] P.M. Nia, P.M. Woi, Y. Alias, Facile one-step electrochemical deposition of copper nanoparticles and reduced graphene oxide as nonenzymatic hydrogen peroxide sensor, Appl. Surf. Sci. 413 (2017) 56–65, https://doi.org/10.1016/j.apsusc.2017.04.043.

[42] S. Zhang, X. Deng, A. Chen, H. Zhou, Z. Xie, Y. Liang, F. Zeng, Facile synthesis of Pd supported on Shewanella as an efficient catalyst for oxygen reduction reaction, Int. J. Hydrogen Energ. 44 (2019) 21759–21768, https://doi.org/10.1016/j.ijhydene.2019.06.141.

[43] Q. Dong, M. Huang, C. Guo, G. Yu, M. Wu, Functionalized titanium carbide as novel catalyst support for Pd catalyzed electrochemical reaction, Int. J. Hydrogen Energy 42 (2017) 3206–3214, https://doi.org/10.1016/j.ijhydene.2016.09.217.

[44] P. Kankla, J. Limtrakul, M.L.H. Green, N. Chanlek, P. Luksirikul, Electrooxidation of formic acid enhanced by surfactant-free palladium nanocubes on surface modified graphene catalyst, Appl. Surf. Sci. 471 (2019) 176–184, https://doi.org/10.1016/j.apsusc.2018.12.001.

[45] D. Xu, D. Fan, W. Shen, Catalyst-free direct vapor-phase growth of $Zn_{1-x}Cu_xO$ micro-cross structures and their optical properties, Nanoscale Res. Lett. 8 (2013) 46, https://doi.org/10.1186/1556-276X-8-46.

[46] D. Zemlyanov, B. Aszalos-Kiss, E. Kleimenov, D. Teschner, S. Zafeiratos, M. Hävecker, A. Knop-Gericke, R. Schlögl, H. Gabasch, W. Unterberger, K. Hayek, B. Klötzer, In situ XPS study of Pd(1 1 1) oxidation. Part 1: 2D oxide formation in 10^{-3} mbar O_2, Surf. Sci. 600 (2006) 983–994, https://doi.org/10.1016/j.susc.2005.12.020.

[47] M.A. Hosseini, S. Malekie, N. Ebrahimi, The analysis of linear dose-responses in gamma-irradiated graphene oxide: Can FTIR analysis be considered a novel approach to examining the linear dose-responses in carbon nanostructures? Radiat. Phys. Chem. 176 (2020) https://doi.org/10.1016/j.radphyschem.2020.109067.

[48] A.D. Pingale, A. Owhal, A.S. Katarkar, S.U. Belgamwar, J.S. Rathore, Facile synthesis of graphene by ultrasonic-assisted electrochemical exfoliation of graphite, Mater. Today-Proc. 44 (2021) 467–472, https://doi.org/10.1016/j.matpr.2020.10.045.

[49] J.C. Ng, C.Y. Tan, B.H. Ong, A. Matsuda, W.J. Basirun, W.K. Tan, R. Singh, B. K. Yap, Novel palladium-guanine-reduced graphene oxide nanocomposite as efficient electrocatalyst for methanol oxidation reaction, Mater. Res. Bull. 112 (2019) 213–220, https://doi.org/10.1016/j.materresbull.2018.12.029.

[50] X. Li, Y.-M. Wang, Y.-L. Wu, H.-R. Wang, M. Chen, H.-D. Sun, L. Fan, Properties and modification mechanism of asphalt with graphene as modifier, Constr. Build. Mater. 272 (2021), https://doi.org/10.1016/j.conbuildmat.2020.121919.

[51] Y. Guo, Z. Li, Y. Xia, Y. Wei, J. Zhang, Y. Wang, H. He, Facile synthesis of ruhtenium nanoparticles capped by graphene and thiols for high-performance supercapacitors, Electrochim. Acta 391 (2021), https://doi.org/10.1016/j.electacta.2021.138990.

[52] M. Baghayeri, H. Alinezhad, M. Tarahomi, M. Fayazi, M.G. Motlagh, B. Maleki, A non-enzymatic hydrogen peroxide sensor based on dendrimer functionalized magnetic graphene oxide decorated with palladium nanoparticles, Appl. Surf. Sci. 478 (2019) 87–93, https://doi.org/10.1016/j.apsusc.2019.01.201.

[53] T.D. Thanh, J. Balamurugan, S.H. Lee, N.H. Kim, J.H. Lee, Novel porous gold-palladium nanoalloy network-supported graphene as an advanced catalyst for non-enzymatic hydrogen peroxide sensing, Biosens. Bioelectron. 85 (2016) 669–678, https://doi.org/10.1016/j.bios.2016.05.075.

[54] M.-M. Liu, W.-T. Wei, Y.-Z. Lu, H.-B. Wu, W. Chen, Synthesis of Graphene-Supported Hollow AgPd Alloy Nanoparticles and the Application in Detection of Hydrogen Peroxide, Chinese J. Anal. Chem. 40 (2012) 1477–1481, https://doi.org/10.1016/S1872-2040(11)60576-8.

[55] Valentin Mirčeski, Andrzej Bobrowski, Jerzy Zarebski, Filip Spasovski, Electrocatalysis of the first and second kind: Theoretical and experimental study in conditions of square-wave voltammetry, Electrochim. Acta 55 (2010) 8696–8703, https://doi.org/10.1016/j.electacta.2010.07.088.

[56] V. Mirčeski, Modification of the step-function method for solving linear integral equations and application in modelling of a voltammetric experiment, J. Electroanal. Chem. 545 (2003) 29–37, https://doi.org/10.1016/S0022-0728(03)00086-X.